Charge Exchange Spectroscopy using Spatial Heterodyne Spectrometer in the Large Helical Device

F. J. Arellano,[1] M. Yoshinuma,[2] and K. Ida[2,3]
[1)] *Center for Atomic and Molecular Technologies, Osaka University, Osaka, Japan*
[2)] *National Institute for Fusion Science, Toki, Japan*
[3)] *The Graduate University for Advanced Studies, SOKENDAI, Toki, Japan*

(*Electronic mail: ida.katsumi@nifs.ac.jp)

(Dated: 1 February 2022)

In this study, the use of a spatial heterodyne spectrometer (SHS) to measure the ion temperature ($T_{C^{6+}}$) and the toroidal flow velocity (V_f) of the C^{6+} impurity ion by charge exchange spectroscopy (CXS) was explored. The instrumental width (IW) of the SHS (aperture size = 16.77 mm^2, etendue = 2.9867 mm^2sr) was extrapolated to be 0.09 nm, which is half of the 0.17 nm IW extrapolated for a conventionally-used dispersive spectrometer (DS) (aperture size = 2.6 mm^2, etendue = 0.2605 mm^2sr). Resulting measurements were found to be in good agreement to those measured using the (DS).

I. INTRODUCTION

The carbon impurity ion temperature ($T_{C^{6+}}$) and the toroidal flow velocity (V_f) in the Large Helical Device (LHD) are typically measured by charge exchange spectroscopy (CXS) using a traditional dispersive spectrometer (DS).[1–3] One disadvantage of employing a DS for CXS is the limitation of the aperture size in order to maintain a high spectral resolution. In a DS, as the input aperture size increases to collect more photons, the spectral resolution becomes significantly poorer. In contrast, a spatial heterodyne spectrometer (SHS) has the advantage of having field-widening prisms that rotate the image of the gratings such that the images are in a virtual plane perpendicular to the optical axis, allowing for a larger aperture size.[4] If the SHS is used, one can increase the number of photons collected without significantly degrading the spectral resolution.

The SHS is an interferometric Fourier transform technique, wherein the measured Fizeau fringe patterns are transformed into spectra by Fast Fourier Transform (FFT). It was originally designed for and mainly used in the measurement of emission lines in astrophysics.[5,6] However, in 2018, Burke et al. reported the possibility of using an SHS to measure the Stark split neutral beam emissions.[7] In a similar way, the use of SHS as a new technique for CXS can therefore be explored. In this study, the potential of using the SHS for CXS in order to achieve a higher optical transmission-to-spectral resolution ratio is investigated. This can be a great advantage in the measurement of the transient ($<$ 1 ms) deviation of the ion velocity distribution from the Maxwell-Boltzmann distribution which occurs during MHD events.[8]

CXS is characterized by the charge transfer from the impurity ions in the plasma to the neutral atoms coming from the neutral beam, leaving the impurity ion in the excited state.[9] For a fully ionized carbon, this reaction is given by

$$H^0_{beam} + C^{6+} \rightarrow H^+ + C^{5+}(n = 8). \quad (1)$$

The spontaneous emission of the excited impurity ion given by C^{5+}(n = 8 $\rightarrow$ 7) emits light at $\lambda = 529.05$ nm. This emitted radiation can then be measured by the spectrometer. From the Doppler broadening and Doppler shift of the spectral line, the $T_{C^{6+}}$ and the V_f can be calculated.

II. EXPERIMENTAL SET-UP

A. SHS in LHD

Fig. 1(a) shows the schematic view of the LHD with the line-of-sight (LOS) of the DS and SHS systems. The LHD is a heliotron device consisting of three tangential beams (NB#1-3) and two perpendicular beams (NB#4-5). The SHS is connected to the lens located at the viewing port 9-O. The neutral beam (NB)#5, which is located at port 1-O, is used to induce the charge exchange reaction corresponding to the SHS measurements. NB#5 is oriented perpendicular to the magnetic flux surface along the major radius. Using mirrors, the LOS of the lens at port 9-O was arranged such that it intersected with NB#5 at an angle of 113.6°. The intersecting region spans from the magnetic axis to the outboard edge of the LHD plasma. However, in this study, SHS measurements were only done in the portion of the intersecting region near the magnetic axis, that is, at R = 3.66 m. The SHS was placed on an anti-vibration table to increase resilience to vibrations.

Charge exchange between fully ionized carbons and thermal neutrals in the plasma produces light emission which overlaps the wavelength range of the target emission. To measure the background emission coming from this charge exchange with the thermal neutrals, NB#5 was modulated on and off. The background emission corresponded to the intensity measured when the beam was off.

For comparison purposes, the intensity of the charge exchange line collected using a DS (Bunkoukeiki Co., Ltd. CLP-400) was also measured. The DS is located at port 6-O, wherein the neutral beam CXS (NBCXS) is induced by NB#4. The LOS of the DS intersects with the NB#4 at an angle of 103°. Similar to the SHS measurements, the DS measurements used in this study were those measured at R = 3.66 m.

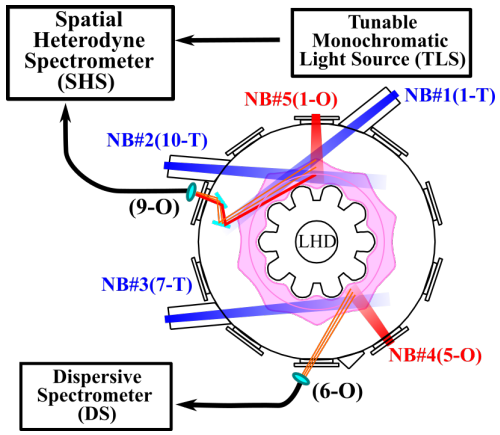

(a) SHS and DS configuration in LHD

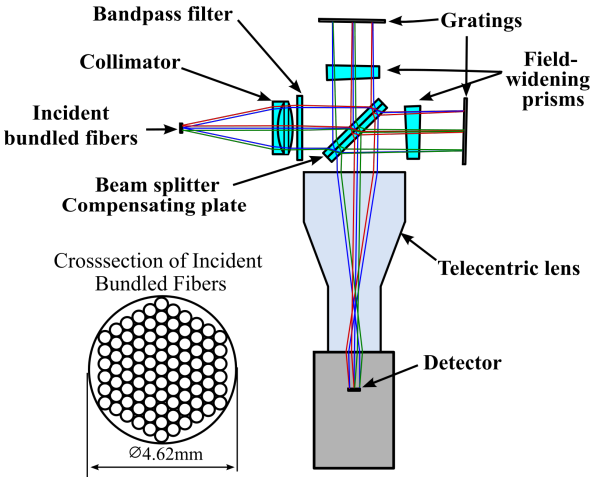

(b) Schematic Diagram of SHS

FIG. 1: SHS configuration

B. Spatial Heterodyne Spectrometer

The set-up of an SHS is fundamentally similar to a Michelson interferometer, but with diffraction gratings instead of mirrors. The SHS (Bunkoukeiki Co., Ltd. BSH-529P) used in this experiment is shown in Fig. 1(b).

The light collected by the lens at the LHD port 9-O is directed to the SHS fiber bundle. This fiber bundle contains 91 fiber cores with a bundle diameter of 4.62 mm. The divergent incident light is then collimated by an achromatic collimator lens and guided to a three-cavity bandpass filter centered at 529.0 nm. After that, the light beam is split into two by the beam splitter and directed to the two gratings. The synthetic quartz compensating plate on the beam splitter was compensated for the variation of optical path induced in one arm. Field widening prisms are inserted between the splitter and the gratings. Upon reaching the gratings, light is diffracted at an angle that is dependent on the wavelength. At a wavelength called the Littrow wavelength, light is returned to the same direction of incidence. The angle of the tilt of the gratings with respect to the optical axis is called the Littrow angle. The SHS used in this study has a tunable Littrow wavelength.

On the way to the detector, light is made to pass through a telecentric lens to reduce perspective errors. For each wavelength that goes through the filter, two wavefronts with a wavelength-dependent crossing angle in between them reach the detector. The superposition of these two wavefronts leads to the formation of a Fizeau fringe pattern. The spatial frequency of the Fizeau pattern is dependent on the corresponding wavelength.

C. SHS Calibration

To calibrate the SHS, the intensity of the light coming from a tunable wavelength monochromatic light source (TLS) was measured and transformed into spectra. The wavelength of the TLS was tuned from 527-530.5 nm. The spectrum width of the monochromatic light can be varied by changing the width of the exit slit of the TLS. Fig. 2(a)-2(c) show the Fizeau fringe image produced at the detector from the light at 528 nm, 529 nm, and 530 nm. The spatial frequency of the fringe patterns is observed to decrease with increasing wavelength. The spectra given in Fig. 2(d) is then derived from the FFT of these fringe patterns. It can be observed that distinct peaks were successfully measured at each specific wavelength value. A zero spatial frequency was measured at 530.8 nm, setting it as the Littrow wavelength.

D. Instrumental Width

The spectral resolution of a spectrometer can be characterized by a parameter called the instrumental width (IW). IW is defined to be the FWHM of the instrumental line profile (ILP).

In this study, the full width at half maximum (FWHM) of the ILP is measured for both SHS and DS by changing the spectrum line width of light from TLS at 529 nm. A single optical fiber is used to transfer the light from TLS to SHS and DS. The FWHM of ILP is extrapolated to be the value of the FWHM when the spectrum line width is zero, and is given in Fig. 3 for both spectrometers.

The almost linear behavior of the fitted line given in Fig. 3 shows a good agreement between the FWHM measured from both spectrometers. Therefore, the SHS has the ability to measure the FWHM correctly as well as a DS does. The IW of the SHS was extrapolated to be 0.09 nm, which is almost half of the IW of the DS (IW = 0.17 nm). Comparing the optical transmission of the two optical systems, the aperture size of the SHS and the DS are calculated to be 16.77 mm^2 and 2.6 mm^2 respectively. Another way to express the optical transmission is through the parameter called etendue (G) which is computed using the equation

$$G = S\sigma = S\frac{\pi}{4F^2} \tag{2}$$

where S is the aperture size, σ is the solid angle, and F is the F-number. The F-number of the SHS and the DS are 2.1

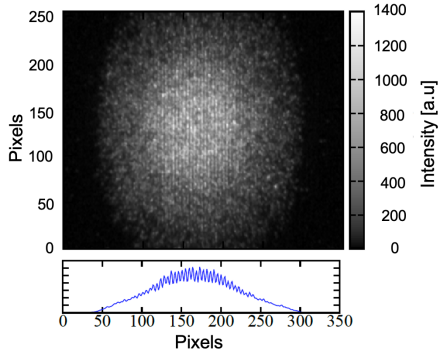

(a) 528nm

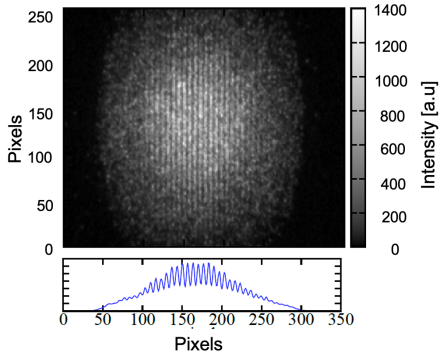

(b) 529nm

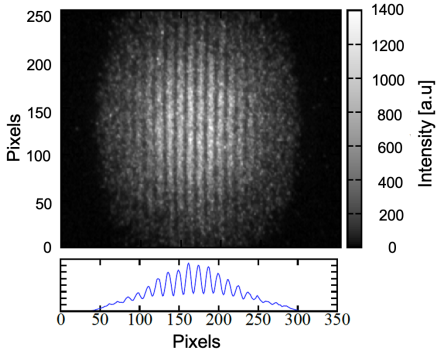

(c) 530nm

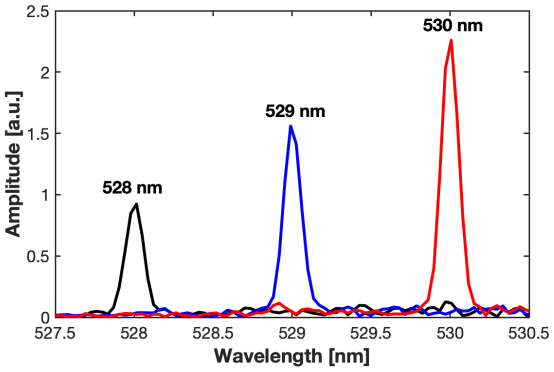

(d) Spectra derived after FFT of interferogram from light source tuned at 528 nm, 529 nm, and 530 nm

FIG. 2: (a-c) Measured fringe pattern and (d) derived spectra from the SHS calibration using a tunable monochromatic light source

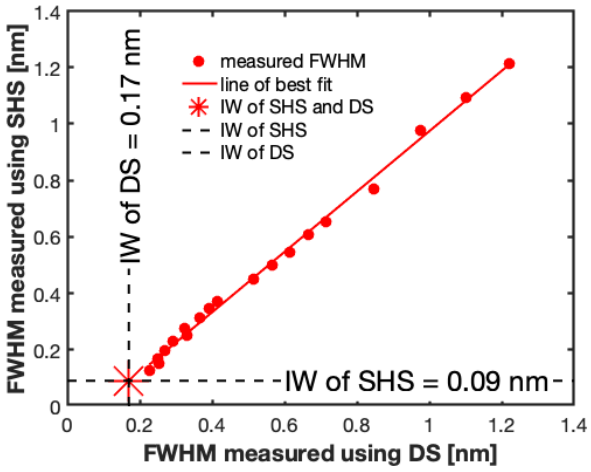

FIG. 3: FWHM measured with SHS and DS along with the IW values

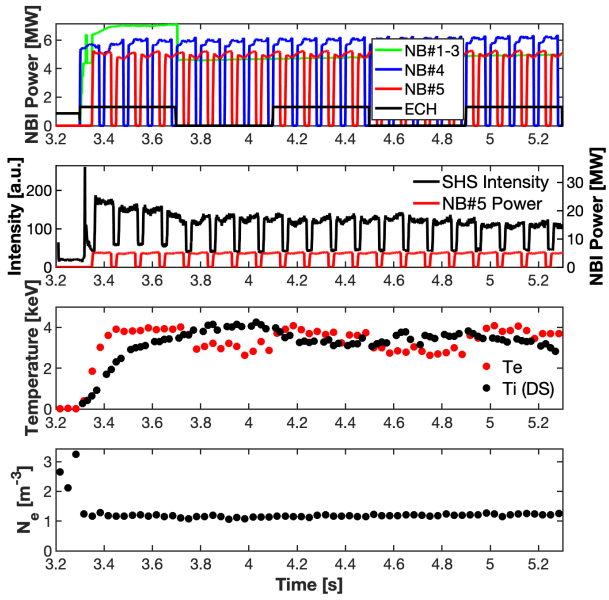

FIG. 4: Parameters of LHD Shot # 164208

and 2.8 respectively. The etendue of the SHS and the DS are therefore calculated to be 2.9867 mm^2sr and 0.2605 mm^2sr respectively. These significant differences in the etendue and the IW presents the SHS as a suitable instrument for the measurements with high spectral resolution and high optical transmission.

III. RESULTS AND DISCUSSION

SHS and DS measurements were done using the Shot # 164208 of the LHD. Fig. 4 shows the discharge characteristics of this shot. The first subfigure in Fig. 4 shows the

beam power of the NB. Here, 'NB#1-3' is the sum of the power from neutral beams 1-3. NB#4, NB#5, and ECH represent the power from NB#4, NB#5, and the electron cyclotron heating (ECH) respectively. It can be seen that during beam modulation, NB#4 and NB#5 were turned on for a longer duration than they were turned off. This allowed for more time-resolved data of the ion parameters. The second subfigure shows the power of the NB#5 plotted alongside the time-dependent intensity derived from the SHS interferogram after FFT. The intensity values were calculated by integrating the spectra from 528.5 nm to 529.7 nm. This shows how the intensity is directly proportional to the NB#5 power. The third and fourth subfigures show the $T_{C^{6+}}$, the electron temperature (T_e) and the electron density (n_e). Here, the T_e and the n_e were measured by Thomson scattering while the $T_{C^{6+}}$ was measured using the DS. The T_e and $T_{C^{6+}}$ are observed to increase and decrease following the ECH modulation.

Fig. 5 shows the resulting SHS interferogram and spectra for Shot # 164208. Measurements were taken at t = 3.4 s (Fig. 5(a)) and t = 4.0 s (Fig. 5(b)). The first subfigures show the raw interferograms directly measured from the SHS. The second subfigures show the intensity derived after FFT('Background+NBCXS'), along with the background emission ('Background'). The background emission is calculated by interpolating neighboring time frames when the NB#5 was turned off. This background emission is then subtracted from the raw intensity to get the CXS intensity induced by NB#5 ('NBCXS Intensity') shown in the third subfigures. The resulting spectra are then fitted to a Gaussian curve.

The Gaussian fit of a spectrum is represented by the equation

$$F(\lambda) = I\exp[-\frac{(\lambda-\lambda_p)^2}{w^2}]+A, \tag{3}$$

where I is the height of the spectrum peak, λ is the corresponding wavelength, λ_p is the peak position, w is the width of the Gaussian curve, and A is the vertical offset from 0. Nonlinear least square fitting was done in order to fit the values of I, λ_p, w, and A into Eq. 3. The V_f and the $T_{C^{6+}}$ can then be calculated from the resulting λ_p and w values. The distance of the λ_p from the standard charge exchange line peak (λ_C) at 529.05 nm yields the Doppler shift. From this value, V_f can be calculated using the equation

$$V_f = c\frac{\mid \lambda_p - \lambda_C \mid}{\lambda_C} \tag{4}$$

where c is the speed of light.

Similarly, w gives the width of the spectrum after Doppler broadening. From this width value, the $T_{C^{6+}}$ is calculated using the equation

$$T_{C^{6+}} = \frac{Am_p[(w^2-w_{SHS}^2)^{0.5}c/\lambda_C]^2}{2}. \tag{5}$$

where A is the atomic mass of carbon, m_p is the proton mass, and w_{SHS} is the Gaussian width induced by instrumental broadening. w_{SHS} is directly related to the IW calculated in Sec. II D. However, in the case of the w_{SHS}, instead of taking

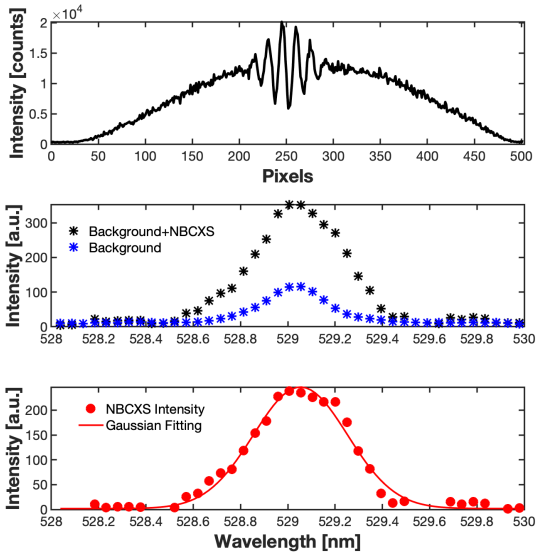

(a) SHS signal and spectra at $T_{C^{6+}}$ = 2.82 keV (t = 3.4 s)

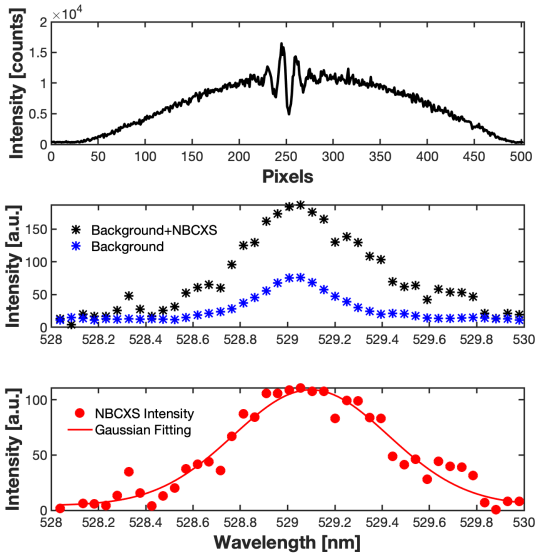

(b) SHS signal and spectra at $T_{C^{6+}}$ = 4.44 keV (t = 4.0 s)

FIG. 5: SHS signal and spectra at $T_{C^{6+}}$ = 2.82 keV and $T_{C^{6+}}$ = 4.44 keV

the FWHM, the half width at the height of e^{-1} is used. w_{SHS} can therefore be calculated using the value of the IW by the equation

$$w_{SHS} = \frac{IW}{2\sqrt{ln2}}. \tag{6}$$

In Fig. 5, the measurements from t = 3.4 s and t = 4.0 s were taken because the calculated $T_{C^{6+}}$ is observed to be lowest at t = 3.4 s and highest at t = 4.0 s. Actually, if the figure is looked

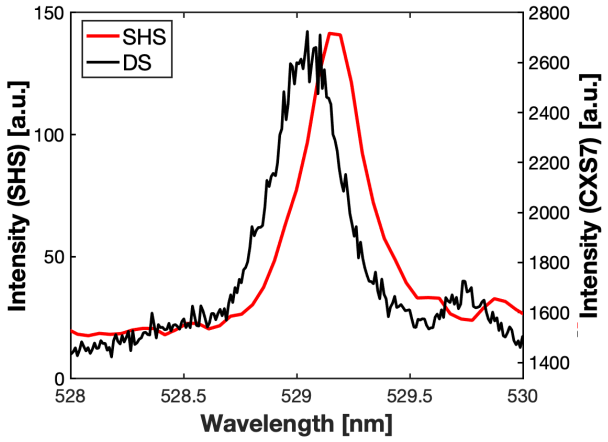

(a) $\lambda_0 = 530.8$ nm

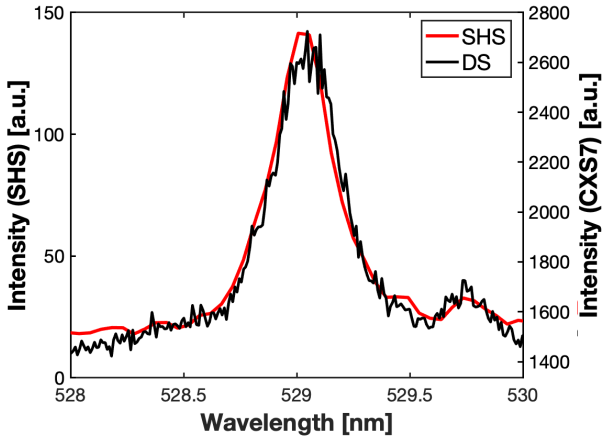

(b) $\lambda_0 = 530.66$ nm

FIG. 6: Wavelength adjustment of SHS spectrum

into closer, one can see that the relative level of the $T_{C^{6+}}$ can already be observed even from the interferogram given on the first subfigure of Fig. 5(a) and Fig. 5(b). Higher sine wave modulation (given at the peak of the interferogram) is present when a lower Doppler width is measured (t = 3.4 s), while a lower sine wave modulation is present at a higher Doppler width (t = 4.0 s). The Doppler width is then observed more clearly after FFT, shown by the width of the spectral line in the second and third subfigures. This observation allows for a relative guess of the $T_{C^{6+}}$ even just from the measured interferograms.

Wavelength values for the derived spectrum are then calculated using the equation

$$\frac{1}{\lambda}[nm^{-1}] = \left(\frac{M\sigma_D}{4\tan\theta - (8\tan\beta_i/n\sigma_0)(dn/d\lambda)} + \sigma_0\right) \times 10^7 \quad (7)$$

where M is the magnification of the telecentric lens, σ_D is the spatial frequency of the waveform (in mm^{-1}), σ_0 is the Littrow wavenumber corresponding to the Littrow wavelength λ_0, n is the refractive index of the grating at λ_0, β_i is the angle of incidence, and $dn/d\lambda$ is the rate of change of the refractive index at λ_0. The resulting SHS spectrum is shown in Fig. 6(a), and is plotted along with that of the DS. Here, the SHS and DS spectra are both passive and were taken at a pulse around t = 4.0 s from another LHD shot (Shot # 163968). From this figure, it can be seen that the peaks of the SHS and DS spectra do not match. The Littrow wavelength used in Eq. 7 is therefore adjusted in such a way that the SHS peaks matched those of the DS, resulting in the figure given in Fig. 6(b). Here, the Littrow wavelength of 530.8 nm measured from the calibration is adjusted to 530.66 nm to match the peaks. The Littrow angle for Eq. 7 is then calculated from this new Littrow wavelength value using the equation

$$\theta = sin^{-1}\left(\frac{N\lambda_0}{2}\right), \quad (8)$$

where N is the grating groove density. This discrepancy of the peaks is attributed to the changes in the Littrow wavelength caused by environmental temperature and pressure changes.

Wavelength adjustment was chosen to be done in such a manner due to the sensitivity of the SHS to environmental conditions. Although the SHS and the DS are measuring the toroidal flow from opposite directions, the position of the DS peak shows that the Doppler shift due to the cold component is < 0.01 nm, which is small compared to the 0.14 nm adjustment applied on SHS spectra.

Fig. 7 shows the resulting time-dependent V_f and $T_{C^{6+}}$ values, along with the values measured from the DS. The V_f and $T_{C^{6+}}$ values from the SHS are averaged for every 20 ms interval. It can be observed that the resulting $T_{C^{6+}}$ measured from the SHS has the same trend and is in good agreement with the $T_{C^{6+}}$ measured by the DS. Both $T_{C^{6+}}$ measurements show the alternating high-low temperature that went with the ECH modulation. V_f values measured from the SHS and DS are observed to be scattered, but the two measurements are found to be in the same range and same general trend. This good agreement shows how the SHS can be used for CXS measurements with the advantage of having a higher resolution at higher optical transmission than a traditional DS.

IV. CONCLUSION

In this study, charge exchange spectroscopy (CXS) in the Large Helical Device (LHD) is performed using a spatial heterodyne spectrometer (SHS) in order to achieve higher spectral resolution even at higher optical transmission. To characterize the spectral resolution, the instrumental width (IW) of the SHS is measured and compared to that of a traditional dispersive spectrometer (DS). The instrumental width of the SHS (IW = 0.09 nm) is extrapolated to be almost half of that of the DS the (IW = 0.17 nm) even though the SHS (aperture size = 16.77 mm^2, etendue = 2.9867 mm^2sr) has a higher optical transmission than the DS (aperture size = 2.6 mm^2, etendue = 0.2605 mm^2sr). Additionally, CXS is used to measure the toroidal flow velocity (V_f) and the ion temperature ($T_{C^{6+}}$) of the C^{6+} impurity present in the LHD. The interferogram measured from the SHS is transformed into spectra using Fourier transform. V_f and $T_{C^{6+}}$ are then calculated from the Doppler

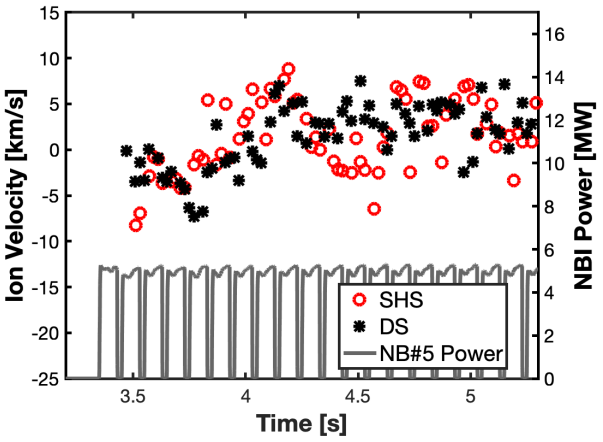

(a) Toroidal flow velocity (V_f)

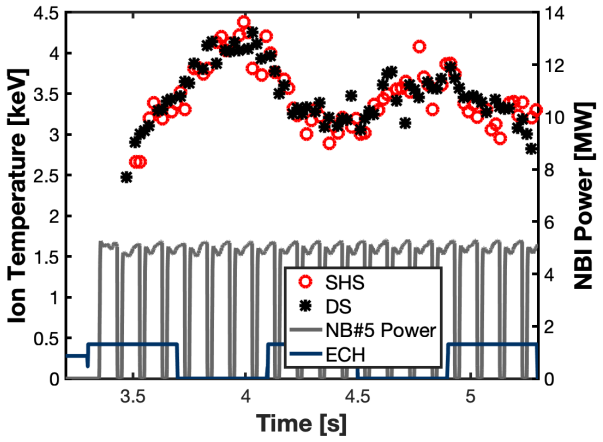

(b) Carbon impurity ion temperature ($T_{C^{6+}}$)

FIG. 7: Toroidal flow velocity (V_f) and carbon impurity ion temperature ($T_{C^{6+}}$)

shift and Doppler width of the Gaussian fitting of the spectra derived. The calculated V_f and $T_{C^{6+}}$ are shown to be in good agreement with the values measured using the DS.

ACKNOWLEDGMENTS

The authors would like to thank the LHD experiment group for their excellent support in this work. This work is supported by Grants-in-Aid for Scientific Research (21H04973 to K.I) of the Japan Society for the Promotion of Science (JSPS).

F.J. Arellano would like to thank Prof. Satoshi Hamaguchi (Osaka University) and the Japan International Cooperation Agency (JICA) Innovative Asia Program for the collaboration opportunity with the National Institute of Fusion Science (NIFS).

The LHD data can be accessed from the LHD data repository at `https://www-lhd.nifs.ac.jp/pub/Repository_en.html`.

[1] T. Ito, M. Osakabe, K. Ida, M. Yoshinuma, M. Kobayashi, M. Goto, S. Murakami, M. Isobe, S. Kobayashi, K. Toi, *et al.*, Rev. Sci. Instrum. **81**, 10D327 (2010).
[2] W.-H. Ko, H. Lee, D. Seo, and M. Kwon, Rev. Sci. Instrum. **81**, 10D740 (2010).
[3] M. Yoshinuma, K. Ida, M. Yokoyama, M. Osakabe, and K. Nagaoka, Fusion Sci. Technol. **58**, 375–382 (2010).
[4] M. Kaufmann, F. Olschewski, K. Mantel, O. Wroblowski, Q. Chen, J. Liu, Q. Gong, D. Wei, Y. Zhu, T. Neubert, *et al.*, CEAS Space J. **11**, 525–531 (2019).
[5] J. M. Harlander and F. L. Roesler, in *Proc. SPIE*, Vol. 1235 (1990) pp. 622–633.
[6] J. Harlander, R. J. Reynolds, and F. L. Roesler, Astrophys. J. **396**, 730–740 (1992).
[7] M. G. Burke, R. J. Fonck, G. R. McKee, and G. R. Winz, Rev. Sci. Instrum. **89**, 10D114 (2018).
[8] K. Ida, T. Kobayashi, M. Yoshinuma, T. Akiyama, T. Tokuzawa, H. Tsuchiya, K. Itoh, and L. E. Group, Phys. Plasmas **24**, 122502 (2017).
[9] R. Isler, Plasma Phys. Control. Fusion **36**, 171–208 (1994).